

Tailoring cryo-electron microscopy grids by photo-micropatterning for in-cell structural studies

Mauricio Toro-Nahuelpan¹, Ievgeniia Zagoriy¹, Fabrice Senger², Laurent Blanchoin^{2,3}, Manuel Théry^{ib}^{2,3} and Julia Mahamid^{ib}^{1*}

Spatially controlled cell adhesion on electron microscopy supports remains a bottleneck in specimen preparation for cellular cryo-electron tomography. Here, we describe contactless and mask-free photo-micropatterning of electron microscopy grids for site-specific deposition of extracellular matrix-related proteins. We attained refined cell positioning for micromachining by cryo-focused ion beam milling. Complex micropatterns generated predictable intracellular organization, allowing direct correlation between cell architecture and in-cell three-dimensional structural characterization of the underlying molecular machinery.

In parallel to the ongoing resolution revolution in cryo-electron microscopy (cryo-EM) for macromolecular structure determination¹, cryo-electron tomography (cryo-ET) has matured to reveal the molecular sociology in situ sensu stricto^{2–4}. Yet, molecular-resolution cryo-ET of adherent mammalian cells can only be directly performed on their thin peripheries (<300 nm). To reveal structures at the cell interior, thinning by cryo-focused ion beam (cryo-FIB) has proved an optimal, artifact-free preparation method^{2,5–12}. Thus, cryo-FIB micromachining coupled to cryo-ET, followed by subtomogram averaging^{13,14}, allows the capture of conformational states and function-related assemblies of macromolecules in cellulose^{4,11,15}. Specimen preparation for cellular cryo-ET, whether performed directly on thin cellular peripheries or following cryo-FIB micromachining, involves seeding of adherent cells on electron microscopy (EM) grids made of a biocompatible metal (for example, gold). Standard EM grids are 3 mm diameter metal meshes overlaid with a delicate perforated thin film. Cells are typically allowed to spread, subjected to genetic or molecular perturbation to represent different physiological settings to be examined in molecular detail and are then arrested by vitrification². However, for cells to be thinned by cryo-FIB, they must be positioned roughly at the center of an individual grid square (Fig. 1a)⁶, and within a few squares away from the grid center. While the first requirement is necessary to allow access to cellular material for ablation by the FIB, the restriction of specimen positioning to the central area of the grid is posed by the subsequent requirement of stage tilt in the transmission electron microscope (TEM) for collection of tomographic tilt series.

Despite a growing number of successfully reported in-cell cryo-ET studies^{4,9,15–18}, controlled on-grid positioning of adherent cells has remained largely unaddressed. Currently, optimization of grids for cellular cryo-ET is primarily carried out by adjusting the concentration of the cell suspension during seeding. Some efforts have also been made by functionalizing grids with extracellular matrix (ECM)-related proteins to promote adhesion of various cell

types^{19–24}; however, adherent cells settle and spread randomly on the homogeneously coated grid films, often in the vicinity or directly on the metal grid bars, making them inaccessible to the FIB or to cryo-ET (Fig. 1a). Furthermore, the presence of large clusters of cells increases the chance of incomplete vitrification due to slower heat transfer from the larger mass of material, and thus deteriorate structural preservation. Such technical hurdles have made the application of state-of-the-art cellular cryo-ET challenging. They further limit the advance of technical developments toward automation and high-throughput sample preparation. Here, we adapted photo-micropatterning, routinely applied to centimeter-scale glass slides for light microscopy-based assays^{25,26}, to develop functionalized EM supports for directing cell positioning at high spatial accuracy, which ultimately render molecular-resolution imaging of frozen-hydrated specimens more easily attainable.

We employed contactless and mask-free photo-micropatterning (Supplementary Fig. 1), ensuring preservation of the delicate support film and precise pattern generation within each grid square. The grids were plasma cleaned, rendering them hydrophilic, and coated with an anti-fouling biologically repelling agent (polyethylene glycol-(PEG)-brush, Supplementary Fig. 1a). Successively, specific areas were ablated with a ultraviolet (UV)-laser, either using a UV-pulsing laser scanned through the grid film on a standard confocal microscope (Supplementary Figs. 1b and 2a–d) or continuous UV-illumination with a digital micro-mirror device (DMD) and a photoactivator (PLPP)²⁷ (Supplementary Fig. 1b'). The DMD provides efficient area coverage of the grid film of approximately 150,000 μm^2 , equivalent to about 3 × 2 grid squares on a 200-mesh grid, and allows creating multiple, complex and precisely positioned PEG-oxidized areas in ~30 s at a resolution of 1.2 μm . The total patterned area can be extended by iterative montages of DMD expositions (Supplementary Fig. 3). Following passivation and patterning, grids can be stored up to 30 d under hydrated conditions at 4 °C. Grids were then functionalized with proteins that facilitated cell adhesion (Supplementary Fig. 1d,e), and can be tailored to support growth and differentiation of various cell types. We demonstrate successful patterning on a variety of grid materials for both the metal mesh and support film (see Supplementary Fig. 3 and Supplementary Discussion for a detailed description). For example, we replaced the commonly used holey amorphous carbon by SiO₂ films^{12,24} (Supplementary Fig. 3a–c), or used an additional layer of thin (2 nm) continuous carbon (on a carbon holey film) to potentially allow for continuous large areas to support cell adhesion (Supplementary Fig. 3d). We also used titanium grids (Supplementary Fig. 3e) instead of the typical gold grids. Titanium

¹Structural and Computational Biology Unit, European Molecular Biology Laboratory, Heidelberg, Germany. ²CytomorphaLab, Interdisciplinary Research Institute of Grenoble, Laboratoire de Physiologie Cellulaire et Végétale, Université Grenoble-Alpes/CEA/CNRS/INRA, Grenoble, France. ³CytomorphaLab, Hôpital Saint Louis, Institut Universitaire d'Hématologie, Université Paris Diderot, Paris, France. *e-mail: julia.mahamid@embl.de

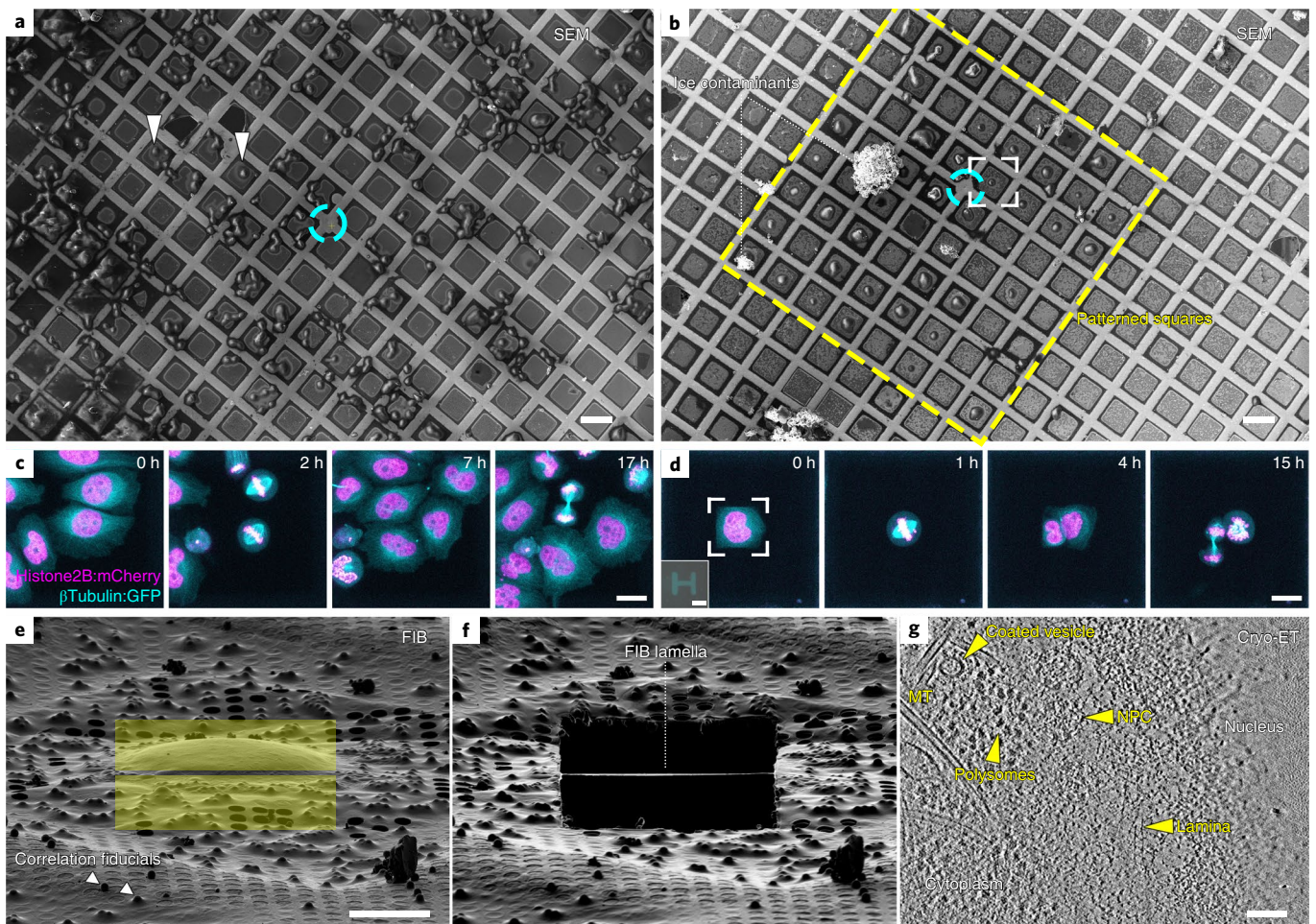


Fig. 1 | Micropatterning of cryo-EM grids refines preparation for cryo-FIB lamella micromachining from adherent mammalian cells. a, Cryo-SEM of HeLa cells grown overnight on a gold-mesh grid with a holey (R2/1) SiO_2 film. Cyan circle indicates grid center. Only a small fraction of the cells is optimally positioned for FIB-lamellae preparation (arrowheads). Scale bar, 100 μm . **b**, HeLa cells grown overnight on a gold-mesh grid coated with a holey (R2/1) carbon film micropatterned with 20 μm diameter disks on 8×8 grid squares (yellow rectangle) around the grid center (cyan circle) and treated with fibronectin. Scale bar, 100 μm . **c,d**, HeLa cells, expressing green fluorescent protein (GFP)-tagged β -tubulin (cyan) and mCherry-tagged histone (H2B, magenta), seeded on a control (**c**) and patterned gold-mesh grids (**d**) with SiO_2 (R1.2/20) holey film. Inset, H-shaped pattern induced the square cell shape. Scale bars, 20 μm . Cell-cycle was synchronized with a single Thymidine block (16 h), released into fresh medium (8 h), followed by overnight live-cell imaging. A field of view of a single grid square is shown for both **c** and **d**. Cells continue dividing ~40 h post-seeding. **e**, FIB shallow angle view on cell framed in **b**. Yellow rectangles indicate patterns for milling. Correlation fiducials (microbeads, arrowheads) can facilitate 3D-targeted cryo-FIB preparations. **f**, Lamella produced from cell in **e**. Scale bar, 10 μm . **g**, Tomographic slice, 6.8 nm thickness, of the nuclear periphery of the cell in **e**. Lamella thickness determined from the tomographic reconstruction was 90 nm. NPC, nuclear pore complex; MT, microtubule. Scale bar 100 nm.

provided more rigid grids, that combined to SiO_2 films, proved to maintain flatness (avoiding cryo-crinkling²⁸), and were more robust for the multiple steps during the micropatterning and cell culture steps (see Methods). Alternatively, all-gold grids (mesh and film, Supplementary Fig. 3f–k) were also successfully patterned and supported cell culture.

HeLa cells are a prominent model system in cell biology, and must be thinned to reveal structures positioned deep in their interior by cryo-ET. HeLa cells were seeded on fibronectin-functionalized micropatterned (30- μm disk-shape) grids. Reproducible seeding of one or two cells at the center of individual grid squares was achieved (Fig. 1b and Supplementary Figs. 2e–g and 3b,c,g–j). Cell viability on micropatterned grids was confirmed by live-cell imaging: time-lapse light microscopy of cell-cycle synchronized cultures showed that cells spread and continue to divide 40 h post-seeding (Fig. 1c,d and Supplementary Video 1). In this case, an H-shape pattern induced cells to adopt a rectangular appearance and can potentially be used to produce defined geometries of cell division and of the

mitotic spindle for structural analysis^{29,30}. Most cells seeded on such grids were directly accessible for FIB thinning (Fig. 1b,e), highlighting the potential of grid micropatterning in streamlining advanced thinning techniques. The presence of microbeads on the grid (Fig. 1e), aimed to be used as fiducials for three-dimensional (3D) cryo-correlative light and electron microscopy (cryo-CLEM)³¹, demonstrates that 3D-targeted FIB preparations could also benefit from spatially controlled cell positioning. Next, electron-transparent lamellae were generated (Fig. 1f and Supplementary Fig. 2g,h)⁶, and cryo-ET on the lamellae produced 3D-tomographic volumes of the nuclear periphery capturing previously described molecular detail⁴ (Fig. 1g). Thus, the developed EM grid micropatterning method offers important advantages for optimization of advanced cellular cryo-ET pipelines, which encompass (1) vitrification, (2) cryo-CLEM, (3) micromachining by cryo-FIB milling and (4) cryo-ET.

Next, we generated complex patterns to control cell shape. Micropatterning on glass surfaces has been previously shown to

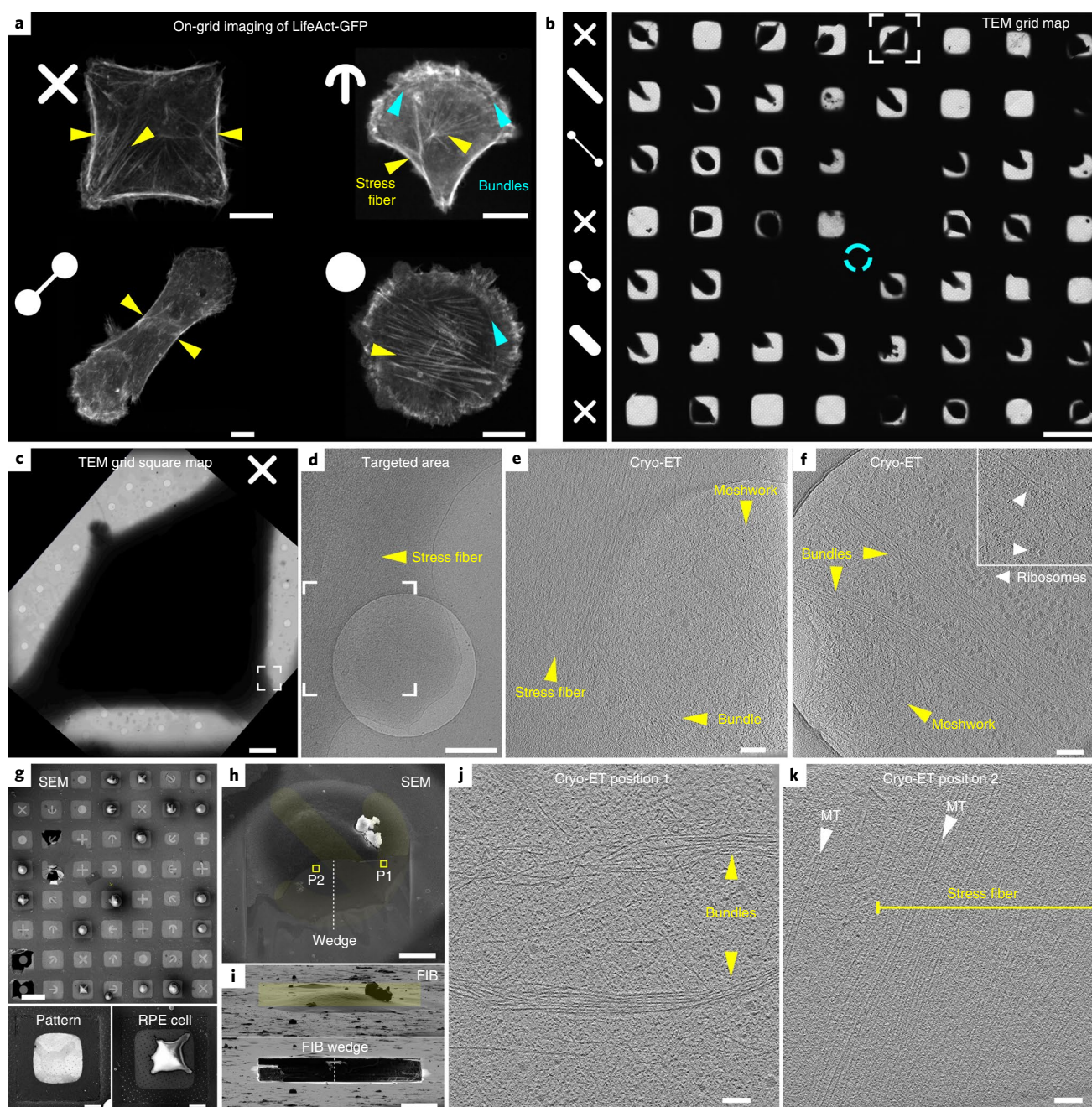


Fig. 2 | Cryo-EM grid micropatterning tailored for controlling cellular morphology and cytoskeletal architecture. **a**, On-grid (gold-mesh, SiO₂ film R1/4) live-cell confocal microscopy of the actin organization in RPE1 LifeAct-GFP cells grown on complex micropatterns. Pattern designs are indicated at the top left of each of the light microscopy images. Positioning of actin stress fibers (yellow arrowheads) correlates with the distinct patterns. Blue arrowheads: actin bundles arranged into an arc or ring structure. Scale bars, 10 μ m. **b-f**, Cellular cryo-ET of RPE1 cells in peripheral thin regions (gold-mesh, SiO₂ film R1/4). **b**, Cryo-TEM map of a grid with 8 \times 7 patterned grid squares. Patterns per row are indicated (left column). Cyan circle, grid center. Scale bar, 100 μ m. **c**, Cryo-TEM micrograph of a grid square of the framed cell in **b** grown on a cross-shaped pattern. Scale bar, 10 μ m. **d**, Magnified cryo-TEM micrograph of the framed area in **c**, targeted for tomography. Scale bar, 500 nm. **e**, Tomographic slice of the specified area in **d**, 6.8 nm thickness, showing the organization of actin filaments into a stress fiber and an isotropic meshwork in the adjacent cellular protrusion. For full tomogram, see Supplementary Video 2. Scale bar, 100 nm. **f**, Tomographic slice of the periphery of another cell grown on an oval-shape pattern depicting actin meshwork, bundles and unidentified hexameric macromolecular complexes in the vicinity of the basal and apical cell membranes (inset, arrowheads). For full tomogram, see Supplementary Video 3. Scale bar, 100 nm. **g-k**, Cellular thinning by cryo-FIB followed by cryo-ET. **g**, SEM of RPE1 cells on a patterned titanium-mesh (SiO₂ film R1.2/20) grid overlaid with an image of the patterns. Scale bar, 100 μ m. Bottom panels; gold-mesh, SiO₂ film R1/4 grid. Left, 2 keV SEM image of a cross-shaped micropatterned grid square. Right, SEM of RPE1 cell spreading on a cross-shaped pattern. Scale bars, 20 μ m. **h**, SEM of a cell grown on a crossbow-shaped pattern (yellow) overlaid with the SEM micrograph of a wedge (top view) produced by cryo-FIB milling (titanium-mesh, SiO₂ film R1.2/20). Squares indicate the positions of tomographic slices in **j** and **k**. Scale bar, 10 μ m. **i**, Upper panel, FIB shallow angle view on cell in **h**. Yellow rectangle indicates the pattern for milling. A thin wedge at the basal cell membrane was produced by ablating the top of the cell. Lower panel, cell after milling. Scale bar, 10 μ m. **j,k**, Tomographic slices of positions 1 and 2 indicated in **h**. Actin bundles likely equivalent to actin transverse arcs (**j**) and internal stress fibers (**k**) are found in locations expected according to the actin map in a crossbow-shaped RPE1 cell (**a**). Scale bars, 100 nm.

induce well-defined cytoskeletal architectures and, as a result, a stereotypical internal organization of the cellular cytoskeleton, as well as organelles^{25,26}. Here, we describe the actin network in Retinal pigment epithelium (RPE1) cells as a proof of principle, which provides a direct readout of the cellular response to adhesion on complex patterns. Complex micropatterns induced reproducible cell morphologies on grids (Fig. 2a)³². Each pattern elicited a distinguishable actin 3D architecture^{26,33,34}, with spatially distinct peripheral and internal stress fibers, transverse arcs and isotropic branched meshworks. To characterize the actin organization underlying these architectures, we first performed cellular tomography directly on the thin peripheries of micropattern-shaped cells (Fig. 2b and Supplementary Fig. 4). A cell grown on a cross-shaped micropattern (Fig. 2c) was chosen aiming to target peripheral actin stress fibers as indicated by the live-cell actin map (Fig. 2a, upper-left). Cryo-TEM of the selected region exhibited a peripheral cellular protrusion and a noticeable stress fiber (Fig. 2d and Supplementary Fig. 5a–d; see Supplementary Fig. 5e–k for additional examined cells). Cryo-ET on the targeted area revealed the presence of a peripheral bundle of aligned actin filaments comprising a stress fiber and the cortical meshwork of a cellular protrusion (Fig. 2e and Supplementary Video 2). Cryo-ET on a different, natively thinner, cell periphery displayed a meshwork of individual actin filaments, exhibiting the expected helical structure (Fig. 2f, Supplementary Fig. 5l,m and Supplementary Video 3). Hexameric macromolecular complexes observed in the vicinity of the basal and apical cell membranes resemble previously reported adhesion-related particles¹⁷ (Fig. 2f, inset).

To explore the organization of the cytoskeleton further away from the cell peripheries and to characterize spatially predictable structures according to live-cell actin maps (Supplementary Fig. 6a,b), we further applied cryo-FIB milling to the micropattern-adherent RPE1 cells. Cryo-scanning electron microscopy (cryo-SEM) of a patterned grid shows the accurate single cell positioning at the centers of individual grid squares (Fig. 2g). Multiple different patterns can be generated on the same grid for direct comparison of different cellular architectures. The patterns' designs can be easily identified by direct imaging with low-voltage SEM or the micropattern-adopted cell shape (Fig. 2g, bottom panels), facilitating the overlay of the pattern design (Fig. 2g, top). An adherent RPE1 cell on a crossbow-shape micropattern was selected for thinning by cryo-FIB (Fig. 2h). Most of the cell material was removed using a single rectangular area (Fig. 2i). This ablates the top of the cell, generating a thin wedge at the basal cell membrane¹². Cryo-ET at positions 1 and 2, indicated on the wedge (Fig. 2h), displayed a curved transverse arc and a stress fiber, respectively (Fig. 2j,k, Supplementary Figs. 6c–e and 7a–d and Supplementary Video 4). Furthermore, microtubules were seen parallel to and, remarkably, fully embedded in the actin stress fiber (Fig. 2k). These structures matched the previously described actin organization in crossbow patterns³³, in which the observed actin bundles likely form part of the transverse arcs, while microtubules were suggested to be aligned with stress fibers at the basal part of the cell (Fig. 2a, upper-right). Thus, this approach provided biological insights on the molecular scale in cellulo, previously described by light microscopy, here unambiguously confirmed by direct visualization of distinct cytoskeleton architectures induced by control of cell morphology. Further data processing by semi-automated segmentation of the tomographic volumes can deliver quantitative 3D structural information, including angular distributions of individual actin filaments and interfilament distances in different cytoskeletal architectures, a level of structural information that is uniquely attainable by cryo-ET³⁵. We further envision that the reproducible internal organization, encompassing positioning of cytoskeletal elements and stereotypical organelles organization in response to predetermined external physical cues posed by the micropatterns (Supplementary Fig. 6f)³³, will

assist in targeting specific internal elements for structural studies without resorting to challenging correlative approaches under cryogenic conditions.

In conclusion, photo-micropatterning of EM grids contributes to the advancement of refined, routine and user-friendly specimen preparations for in-cell structural biology. It further aids in solving technical challenges that have, thus far, hindered high-throughput FIB thinning preparations. This method has great potential for developing automation of the cryo-FIB milling process, deeply impacting the streamlining of the cellular cryo-EM pipeline. It offers a unique opportunity to generate in-cell integrated insight into the structural dynamics of macromolecules at nanometer-scale, broadening the scope of questions that can be addressed by state-of-the-art structural biology methods and bridging to other life-science disciplines.

Online content

Any methods, additional references, Nature Research reporting summaries, source data, extended data, supplementary information, acknowledgements, peer review information; details of author contributions and competing interests; and statements of data and code availability are available at <https://doi.org/10.1038/s41592-019-0630-5>.

Received: 19 June 2019; Accepted: 7 October 2019;

Published online: 18 November 2019

References

- Kühlbrandt, W. The resolution revolution. *Science* **343**, 1443–1444 (2014).
- Pfeffer, S. & Mahamid, J. Unravelling molecular complexity in structural cell biology. *Curr. Opin. Struct. Biol.* **52**, 111–118 (2018).
- Beck, M. & Baumeister, W. Cryo-electron tomography: can it reveal the molecular sociology of cells in atomic detail. *Trends Cell Biol.* **26**, 825–837 (2016).
- Mahamid, J. et al. Visualizing the molecular sociology at the HeLa cell nuclear periphery. *Science* **351**, 969–972 (2016).
- Schaffer, M. et al. Optimized cryo-focused ion beam sample preparation aimed at in situ structural studies of membrane proteins. *J. Struct. Biol.* **197**, 73–82 (2017).
- Rigort, A. et al. Focused ion beam micromachining of eukaryotic cells for cryoelectron tomography. *Proc. Natl Acad. Sci. USA* **109**, 4449–4454 (2012).
- Wang, K., Strunk, K., Zhao, G., Gray, J. L. & Zhang, P. 3D structure determination of native mammalian cells using cryo-FIB and cryo-electron tomography. *J. Struct. Biol.* **180**, 318–326 (2012).
- Hariri, H. et al. Mdm1 maintains endoplasmic reticulum homeostasis by spatially regulating lipid droplet biogenesis. *J. Cell Biol.* **218**, 1319–1334 (2019).
- Ader, N. R. et al. Molecular and topological reorganizations in mitochondrial architecture interplay during Bax-mediated steps of apoptosis. *eLife* **8**, e40712 (2019).
- Khanna, K. et al. The molecular architecture of engulfment during *Bacillus subtilis* sporulation. *eLife* **8**, e45257 (2019).
- Weiss, G. L., Kieninger, A. K., Maldener, I., Forchhammer, K. & Pilhofer, M. Structure and function of a bacterial gap junction analog. *Cell* **178**, 374 e315–384.e15 (2019).
- Jasnin, M., Ecke, M., Baumeister, W. & Gerisch, G. Actin organization in cells responding to a perforated surface, revealed by live imaging and cryo-electron tomography. *Structure* **24**, 1031–1043 (2016).
- Asano, S., Engel, B. D. & Baumeister, W. In situ cryo-electron tomography: a post-reductionist approach to structural biology. *J. Mol. Biol.* **428**, 332–343 (2016).
- Förster, F. & Hegerl, R. Structure determination in situ by averaging of tomograms. *Methods Cell Biol.* **79**, 741–767 (2007).
- Guo, Q. et al. In situ structure of neuronal C9orf72 poly-GA aggregates reveals proteasome recruitment. *Cell* **172**, 696–705 (2018).
- Bäuerlein, F. J. B. et al. In situ architecture and cellular interactions of PolyQ inclusions. *Cell* **171**, 179–187 (2017).
- Patla, I. et al. Dissecting the molecular architecture of integrin adhesion sites by cryo-electron tomography. *Nat. Cell Biol.* **12**, 909–915 (2010).
- Marston, D. J. et al. High Rac1 activity is functionally translated into cytosolic structures with unique nanoscale cytoskeletal architecture. *Proc. Natl Acad. Sci. USA* **116**, 1267–1272 (2019).

19. Siegmund, S. E. et al. Three-dimensional analysis of mitochondrial crista ultrastructure in a patient with leigh syndrome by in situ cryoelectron tomography. *iScience* **6**, 83–91 (2018).
 20. Sorrentino, S., Studt, J. D., Horev, M. B., Medalia, O. & Sapra, K. T. Toward correlating structure and mechanics of platelets. *Cell Adh. Migr.* **10**, 568–575 (2016).
 21. Tamir, A. et al. The macromolecular architecture of platelet-derived microparticles. *J. Struct. Biol.* **193**, 181–187 (2016).
 22. Hampton, C. M. et al. Correlated fluorescence microscopy and cryo-electron tomography of virus-infected or transfected mammalian cells. *Nat. Protoc.* **12**, 150–167 (2017).
 23. Mader, A., Elad, N. & Medalia, O. Methods in enzymology. *Methods Enzymol.* **483**, 245–265 (2010).
 24. Maimon, T., Elad, N., Dahan, I. & Medalia, O. The human nuclear pore complex as revealed by cryo-electron tomography. *Structure* **20**, 998–1006 (2012).
 25. Azioune, A., Carpi, N., Tseng, Q., Thery, M. & Piel, M. Methods in cell biology. *Meth. Cell Biol.* **97**, 133–146 (2010).
 26. Thery, M. Micropatterning as a tool to decipher cell morphogenesis and functions. *J. Cell Sci.* **123**, 4201–4213 (2010).
 27. Strale, P. O. et al. Multiprotein printing by light-induced molecular adsorption. *Adv. Mater.* **28**, 2024–2029 (2016).
 28. Booy, F. P. & Pawley, J. B. Cryo-inking: what happens to carbon films on copper grids at low temperature. *Ultramicroscopy* **48**, 273–280 (1993).
 29. Thery, M., Jimenez-Dalmaroni, A., Racine, V., Bornens, M. & Julicher, F. Experimental and theoretical study of mitotic spindle orientation. *Nature* **447**, 493–496 (2007).
 30. Thery, M. et al. The extracellular matrix guides the orientation of the cell division axis. *Nat. Cell Biol.* **7**, 947–953 (2005).
 31. Arnold, J. et al. Site-specific cryo-focused ion beam sample preparation guided by 3D correlative microscopy. *Biophys. J.* **110**, 860–869 (2016).
 32. Engel, L. et al. Extracellular matrix micropatterning technology for whole cell cryogenic electron microscopy studies. *J. Micromech. Microeng.* **29**, 115018 (2019).
 33. Thery, M. et al. Anisotropy of cell adhesive microenvironment governs cell internal organization and orientation of polarity. *Proc. Natl Acad. Sci. USA* **103**, 19771–19776 (2006).
 34. Senger, F. et al. Spatial integration of mechanical forces by α -actinin establishes actin network symmetry. *J. Cell Sci.* <https://doi.org/10.1242/jcs.236604> (2019).
 35. Jasnin, M. & Crevenna, A. H. Quantitative analysis of filament branch orientation in listeria actin comet tails. *Biophys. J.* **110**, 817–826 (2016).
- Publisher's note** Springer Nature remains neutral with regard to jurisdictional claims in published maps and institutional affiliations.
- © The Author(s), under exclusive licence to Springer Nature America, Inc. 2019

Methods

A supplementary protocol detailing the method reported here is available at ref. ³⁶.

Cell lines and culture. Wild type HeLa Kyoto cells, and a double tagged line expressing both green fluorescent protein (GFP)-tagged β -tubulin from a bacterial artificial chromosome and mCherry-tagged histone from a plasmid construct (H2B-mCherry), were kindly provided by the Hyman Laboratory, Max Planck Institute of Molecular Cell Biology and Genetics. HeLa cells were cultured in Dulbecco's modified Eagle's medium (DMEM GlutaMAX, ThermoFischer Scientific), while RPE1 (Retinal Pigment Epithelial human cells) expressing LifeAct-GFP³⁷ were cultured in DMEM F-12 GlutaMAX. Cells were incubated at 37°C with 5% CO₂, and supplemented with 10% (v/v) fetal bovine serum (FBS), 100 mg ml⁻¹ penicillin, 100 mg ml⁻¹ streptomycin. A 0.5 mg ml⁻¹ gentamicin (G418) for the bacterial artificial chromosome-tagged lines and puromycin (1 μ g ml⁻¹) for cells carrying the plasmids were used. FluoroBrite DMEM supplemented with 2 mM L-glutamine (ThermoFischer Scientific) was used for live-cell fluorescence imaging.

EM grids. Gold (Au) mesh grids with a holey 12 nm thick film made of SiO₂ (R1.2/20, R1/4, hole size/spacing in μ m), amorphous carbon (R2/1) or 50 nm gold film (UltraAuFoil, R2/2) were used. A gold mesh with a continuous thin layer (2 nm) of amorphous carbon placed on top of a holey (R2/1) carbon film was also employed. In addition, we used titanium (Ti) grids with a holey (R1.2/20) 12 nm thick SiO₂. All grids were 200-mesh and purchased from Quantifoil Micro Tools. For detailed description of the different grid materials for mesh and support, see Supplementary Discussion.

Grid passivation. One-step. Grids were oxidized and rendered hydrophilic using a low-pressure plasma cleaning (Diener Femto Plasma, DienerElectronic). Grids were placed onto a glass slide and both sides were plasma cleaned at 100 W power with a 10 cm³ per min flow rate of oxygen gas for 30–40 s. Next, grids were incubated on droplets of poly-L-lysine grafted with polyethylene glycol (PLL(20)-g[3.5]-PEG(5), SuSoS AG) at a concentration of 0.5 mg ml⁻¹ in 10 mM Hepes pH 7.4, for 1 h at room temperature or overnight at 4°C, on parafilm in a humid chamber (parafilm sealed dish with soaked filter paper). Following passivation, the grids were blotted with filter paper from the back, allowed to dry for few seconds and immediately placed on a drop of the next micropatterning solution (depending on the micropatterning method) in a sealed glass bottom ibidi μ -Dish 35 mm low (ibidi).

Two-step. As an alternative, a two-step treatment of the grids was also tested. First, grids were plasma cleaned, and then incubated on droplets of 0.01% PLL (Sigma Aldrich) on parafilm in a humid chamber overnight at room temperature. Next, the grids were rinsed five times in 100 mM NaHCO₃, pH 8.4, and incubated for 1–2 h with 50 mg ml⁻¹ PEG-sva dissolved in the same solution (Laysan Bio). Subsequently, the grids were washed five times in 100 mM NaHCO₃, pH 8.4. This treatment can be potentially applied in the absence of a plasma cleaner.

Both protocols were successful for grid passivation followed by photo-micropatterning, as judged from fluorescence light microscopy imaging of GFP-adsorption that was restricted to the PEG-free patterns. However, a one-step PLL-g-PEG passivation was preferred for time consideration.

Micropattern design. Micropatterns were designed in Inkscape (<http://www.inkscape.org/>) as 8-bit binary files and exported as .png files, which can be loaded into the Leonardo software v.4.12 (Alvéole Laboratory).

Micropatterning and functionalization of grids. Nanoablation by a 355 nm pulse laser. An inverted confocal Olympus FluoView 1200 (Olympus) microscope was used, equipped with a UV pulsed laser source of 355 nm (PNV-001525-140, Teem Photonics), a UPLSAPO \times 63 (numerical aperture (NA) 1.35) oil objective and a standard photomultiplier or GaAsP photomultiplier detectors. The 355 nm laser had an average power of 50 mW, 500 ps pulse width, 1 kHz repetition rate and a maximum energy per pulse of 30 μ J. After passivation with PLL-g-PEG, grids were blot-dried from the back with a filter paper and quickly placed with the SiO₂ film facing down (toward the objective) on 1–3 μ l of Hepes 10 mM pH 7.4 or PBS in a sealed glass bottom ibidi μ -Dish 35 mm low (ibidi). High humidity was kept using water-soaked filter paper inside the dish to avoid solution evaporation during micropatterning. Transmission and reflection were observed with a 488 nm laser. The patterns (regions of interest) were of square or circular shape (20, 30 or 40 μ m diameter) generated using the Olympus FV 10-ASW software v.04.02.03.02. Photo-micropatterning was performed using 10–11% laser power, 40 μ s per pixel and ten iterations. Individual grid squares were targeted at a time, the film focused and the laser applied. Micropatterning of a 4 \times 4 grid squares area (200-mesh grid: \sim 260,000 μ m²) took approximately 8 min. Potentially, a lower magnification objective can be used to pattern more grid squares at the same time to optimize patterning, provided that the film is flat and at even height to maintain all areas in the focus plane. Titanium grids had a consistent film flatness aiding quick focusing on each grid square, facilitating the micropatterning using this technique.

PRIMO (DMD-based illumination and photoactivator). An inverted Nikon microscope Ti-E equipped with a CFI Super Plan Fluor 20 \times ELWD (NA 0.45) lens with high UV-transmission, a Perfect Focus System 3, an ORCA-Flash 4.0 LT CMOS camera (Hamamatsu), a motorized stage (Märzhäuser) and the Primo micropatterning module (Alvéole Lab) was used. Grid micropatterning was performed using a DMD to generate a spatially controlled laser illumination of the sample (Primo, Alvéole Lab), with a resolution limit of \sim 1.2 μ m. After passivation with PLL-g-PEG, grids were blot-dried from the back with a filter paper and quickly placed on a 1–3 μ l of PLPP (4-benzoylbenzyl-trimethylammonium chloride, 14.5 mg ml⁻¹) drop in a sealed glass bottom ibidi μ -Dish 35 mm low (ibidi). High humidity was kept using water-soaked filter paper inside the dish to avoid PLPP evaporation. The dish, with 1–4 grids at a time, was placed on the microscope stage and photo-patterning was controlled with the μ manager software v.1.4.22 by the Leonardo plugin software v.4.12 (Alvéole Lab) using the stitching mode and a 375 nm (4.5 mW) laser, applying a dose of 800–1,000 mJ mm⁻² equivalent to \sim 30 s per DMD exposition. Micropatterning of 8 \times 7 grid squares area (200-mesh grid: \sim 900,000 μ m²) took 3–7 min depending on the total dose and grid positioning with respect to the DMD mirror illumination. Grids were promptly retrieved from the PLPP solution, washed in a 1,000 μ l drop of water and two consecutive washes in 300 μ l drops of PBS. Patterned one-step passivated grids were stored wet in PBS at 4°C in a humid chamber, remaining functional for at least 30 d.

Grid functionalization. For functionalization following PEG ablation in micropatterns using both methods, grids were incubated at room temperature for 1 h in a 20 μ l drop of 100 μ g ml⁻¹ of GFP, 50 μ g ml⁻¹ fibronectin (ThermoFischer Scientific) or 30 μ g ml⁻¹ of fibrinogen-Alexa546 (ThermoFischer Scientific) on parafilm and, subsequently, washed three times in 300 μ l drops of PBS. Fibrinogen was prepared in 100 mM NaHCO₃, pH 8.4, hence washes were performed in the same buffer. Grids incubated with fibronectin remained functional for at least 10 d in PBS at 4°C in a humid chamber. The maximum active life time of the micropatterned grids, as well as protein functionalization remain unknown, as this will also depend on the protein stability itself.

All patterning steps and grid treatments were performed under sterile conditions using a Bunsen burner. Grids were handled with a tweezer no. 55 (Dumont).

Comparison between the two patterning approaches. Due to the pulsing nature of the laser in the first approach, it has to scan the region of interest to ablate the anti-fouling agent. The action of the laser leaves an impression on the film that is visible by light microscopy (Supplementary Fig. 2a,b). The engraving can be further observed in detail by FIB (side view) and SEM (top view) imaging of a grid square (Supplementary Fig. 2c,d). The film engraving at the conditions used did not seem to cause a deterioration of the SiO₂ layer. In fact, proper cell adhesion to the fibronectin-coated patterns (Supplementary Fig. 2e,f) and the subsequent vitrification of grids appeared unaltered (Supplementary Fig. 2g). Furthermore, followed by cell settling on the patterns, they strictly adhere and divide on the micropatterned regions (Supplementary Fig. 2f), denoting cell viability and the effectiveness of the passivation. Some agglomeration of cells can be appreciated in the Supplementary Fig. 2e. This can be overcome by optimizing cell seeding conditions using fewer cells per cm² and shorter time of seeding (earlier transfer to a new cell-free dish), along with use of a cell strainer. Using this method, a directed spatial positioning of cells was attained, which was valuable for cryo-FIB milling (Supplementary Fig. 2g–j), demonstrating and further supporting the advantages of micropatterning for the cellular cryo-ET pipeline optimization.

While the Primo device takes 30 s per DMD run (for a dose of 1,000 mJ mm⁻² and covering a 3 \times 2 grid squares on a 200-mesh grid), the 355 nm pulse laser patterning takes \sim 10–15 s per grid square considering a disk-shaped pattern of 20–30 μ m diameter. A user familiar with the 355 nm laser technique can pattern a 4 \times 4 grid square area in \sim 8 min. The Primo technology covers a similar area in \sim 1 min.

The 355 nm pulse scanning laser can yield spatial lateral resolution limited by the light diffraction limit equivalent to \sim 250 nm, in comparison to the Primo performance that is limited to \sim 1.2 μ m.

Cell seeding. Nonpatterned grids were plasma cleaned. Cells were detached from cell culture flasks using 0.05% trypsin-EDTA and seeded on pretreated (either patterned or nonpatterned) grids in glass bottom ibidi μ -Dish 35 mm high (ibidi).

Cells were seeded on fibronectin micropatterned surfaces right after being passed through a cell 40 μ m pore-size cell strainer (Corning) at a density of 2 \times 10⁴ cells per cm² for HeLa and 8 \times 10³ cells per cm² for RPE1 cell lines. After seeding, grids were incubated for 1.5–2 h for HeLa cells or 20–35 min for RPE1 cells. Next, grids were transferred to a new cell-free dish and incubated at 37°C with 5% CO₂ to allow cell adhesion to the grids. Transfer to a new dish was beneficial to remove cells that were nonspecifically attached to areas outside the patterns. Cells were vitrified 4–6 h post-transfer for RPE1 cells (to attain a higher number of grid squares with single cells) or after overnight incubation for HeLa cells.

At least 60 grids have been seeded with either HeLa or RPE1 cells obtaining reproducible results with cells settling and adhering to the micropatterned areas.

Live-cell confocal imaging. Cell-cycle synchronization was aimed at validating cell viability after adhesion on micropatterned grids by live-cell imaging. HeLa cells were allowed to adhere overnight (16 h) in the presence of 2 mM thymidine (S-phase block, Merck) and released into fresh medium. Imaging started 8 h post-release and time-lapse videos were recorded overnight.

Time-lapse imaging of HeLa cells on grids (Fig. 1c,d) was performed on a Zeiss LSM 880 AiryScan microscope (Carl Zeiss) using confocal detectors and a Plan-Apochromat $\times 20$ (NA 0.8) objective. Field of view was $425 \times 425 \mu\text{m}^2$, pixel size was 149 nm and z-step size was 1 μm (total z-depth, 32 μm). Pixel dwell time: was 0.28 μs and master gain was 850 for both channels. GFP was detected using a 488 nm line of argon laser with a power of 1.5% and a 490–550 nm bandpass emission filter. mCherry was detected using a 561 nm diode-pumped solid-state laser at a 0.15% power, and a bandpass emission filter of 570–660 nm. Time-lapse imaging was performed with 1 h time resolution using Zen Black 2.3 SP1 software v.14.0.15.201 and the MyPic Visual Basic macro³⁸. The xz images of the dish surface reflection was acquired and processed by the MyPic Visual Basic macro to define the axial position for z-stack acquisition at each time point. Each stack was post-processed in Fiji³⁹. Briefly, channels were split, maximum intensity projections produced, channels combined into a single image per time point and all time points combined into a video stack.

Zeiss AiryScan microscopy. AiryScan microscopy of RPE1 cells on patterned grids (Fig. 2a) was performed on a Zeiss LSM 880 AiryScan microscope (Carl Zeiss), using an AiryScan detector and a C-Apochromat $\times 40$ (NA 1.2) water immersion objective. Optimal sampling conditions for AiryScan acquisitions were achieved by selecting the super-resolution scanning modality: a pixel size of 50 nm and a 225 nm z-step (total z-depth, 10–15 μm), pixel dwell time was 0.64–1.18 μs and master gain was 850–900. LifeAct-GFP was detected using a 488 nm line of Argon laser with a power of 1.5–2% and a 495–550 nm bandpass emission filter. Stack datasets were post-processed in Zen Black 2.3 SP1 software v.14.0.15.201 (Zeiss) to combine the multiple AiryScan 32-detector array images into deconvolved final images with high signal-to-noise ratio and resolution.

Widefield microscopy imaging. Epifluorescence images (Fig. 2d inset and Supplementary Fig. 2) were recorded using a Zeiss Axio Observer.Z1 widefield microscope (Carl Zeiss) with an AxioCam MRm CCD camera, a A-Plan $\times 10$ (NA 0.25) Ph1 and a LD-Plan Neofluar $\times 20$ (NA 0.4) Ph2 Corr objectives. GFP was imaged with a 38 HE filter set and mCherry with a 43 HE filter set. Cells were imaged at 37°C and 5% CO₂ with the Zen (blue edition) 2.3 software v.2.3.69.1000. Images were processed (histogram adjusted and cropped) in Fiji.

Vitrification. Grids were blotted from the reverse side of the film and immediately plunged into a liquid ethane or ethane/propane mixture at liquid nitrogen temperature using a Leica EM GP plunger (Leica Microsystems). The plunger was set to 37°C, 99% humidity and blot times of 2 s for R2/1, R2/2 and 2.5 s for the R1/4 and R1.2/20 grids. The frozen grids were stored in sealed boxes in liquid nitrogen until further processing.

Cryo-SEM and FIB. Cryo-FIB lamella preparations was performed as described in ref. ⁵, on a dedicated Aquilos dual-beam microscope equipped with a cryo-transfer system and a cryo-stage (ThermoFisher Scientific). Plunge frozen grids were fixed into autogrids modified for FIB preparation (a generous gift from the Max Planck Institute of Biochemistry), mounted into a shuttle (ThermoFisher Scientific) and transferred into the dual-beam microscope via a load-lock system. During FIB operation, samples were kept at constant liquid nitrogen temperature using an open nitrogen-circuit, 360° rotatable cryo-stage. To improve sample conductivity and reduce curtaining artifacts during FIB milling, the samples were first sputter coated with platinum in situ (10 mA, 20 s), and then coated with organometallic platinum using the in situ gas injection system (ThermoFisher Scientific) operated at room temperature, 10.6 mm stage working distance and 7 s gas injection time. Appropriate positions for FIB preparations were identified and recorded in the MAPS 3.3 software (ThermoFisher Scientific), and the eucentric height refined per position. Lamellae or wedges were prepared using a gallium ion beam at 30 kV, stage tilt angles of 20° for lamellae and 12–13° for wedges. Lamella or wedge preparations were conducted in a stepwise manner, starting 5 μm away from the area of interest with currents of 1 nA, gradually reduced to a current of 50 pA for the final cleaning steps. Progress of the milling process was monitored using the scanning electron beam operated at 10 keV and 50 pA (or 2 keV for visualization of micropatterns). For improved conductivity of the final lamella for specimens intended for phase plate tomography, we again sputter coated the grid after cryo-FIB preparation with platinum (10 mA, 3 s). Grid were stored in sealed boxes in liquid nitrogen until further processing.

Cryo-ET. Cryo-EM data were collected on a Titan Krios microscope operated at 300 kV (ThermoFisher Scientific) equipped with a field-emission gun, a Quantum post-column energy filter (Gatan), a K2 Summit direct detector camera (Gatan) and a Volta phase plate (VPP) (ThermoFisher Scientific). Data were recorded in dose-fractionation mode using acquisition procedures in SerialEM software v.3.7.2 (ref. ⁴⁰). Before the acquisition of tilt-series, montages of the grid squares or lamella

were acquired at ~ 2 nm per pixel. Tilt-series using a dose symmetric scheme⁴¹ were collected in nano-probe mode, EFTEM magnification $\times 42,000$ corresponding to pixel size at the specimen level of 3.37 Å, 3–4 μm defocus, tilt increment 2° with constant dose for all tilts, total dose of $\sim 120 \text{ e}^-$ per Å². The pre-tilt of lamellae with respect to the grid plane due to cryo-FIB milling at shallow angles (10–15°) was corrected for by tilting the stage on the microscope. Conventional tilt-series, without a VPP, were acquired with an objective aperture and a beam tilt of 4 mrad for autofocusing (tomograms in Fig. 2e and f and Supplementary Fig. 5). A fraction of the tomographic tilt-series was acquired with the VPP (tomograms in Fig. 1g and Fig. 2j,k). Alignment and operation of the VPP were essentially carried out as described previously, applying a beam tilt of 10 mrad for autofocusing⁴. For conventional defocus data, a total of 30 tomograms were acquired on the peripheral areas of 13 micropatterned cells (from all micropattern designs shown in Fig. 2b). A total of 31 VPP tomograms were acquired from eight wedges, equivalent to eight cells grown on crossbow-, cross-, dumbbell-, oval- and disk-shaped micropatterns.

Data processing. Before tilt-series alignment, the projection movies were corrected for beam-induced drift in the SerialEM plugin. Tilt-series alignment and tomographic reconstructions were performed using the IMOD software package v.4.9.0 (ref. ⁴⁰). In the absence of fiducial gold nanoparticles in the FIB-lamellae or wedges, alignment of tilt-series images was performed with patch-tracking. Final alignment of the tilt-series images was performed using the linear interpolation option in IMOD without CTF correction. Aligned images were binned to the final pixel size of 13.48 Å. For tomographic reconstruction, the radial filter options were left at their default values (cut off, 0.35; fall off, 0.05). Tomograms from Fig. 2e and Supplementary Fig. 5d were treated with an anisotropic nonlinear diffusion denoising algorithm implemented in IMOD.

Statistics and reproducibility. Experiments performed in Figs. 1a,b,e–g, 2a,g–k, Supplementary Figs. 2a,b,e,f, 3a–j, 6a,c–e and 7a–d and Supplementary Video 4 were performed independently three times with similar results.

Experiments from Fig. 1c,d and Supplementary Video 1 were performed once in a non-patterned and a patterned grid, time lapses were collected in five areas of the patterned grid, each area covering multiple grid squares.

Experiments from Fig. 2b–f, Supplementary Fig. 4a–c, Supplementary Fig. 5a–m, and Supplementary Videos 2 and 3, were performed in triplicate (three grids), collecting tomographic data from only one grid, resulting in 30 tomograms from 13 cells. Imaging by FIB–SEM of patterned grids (with laser 355 nm) in Supplementary Fig. 2c,d was performed only once. Experiments in Supplementary Fig. 2g–j was independently performed twice. In the Supplementary Fig. 3k, one grid (out of three grids) was used for cellular thinning by cryo-FIB milling.

Reporting Summary. Further information on research design is available in the Nature Research Reporting Summary linked to this article.

Data availability

The authors declare that the data supporting the findings of this study are available within the paper and its Supplementary Information files. The raw data are available from the corresponding author upon reasonable request.

References

- Toro-Nahuelpan, M. et al. *Prot. Exch.* <https://doi.org/10.21203/rs.2.12377/v1> (2019).
- Vignaud, T. et al. Reprogramming cell shape with laser nano-patterning. *J. Cell Sci.* **125**, 2134–2140 (2012).
- Politi, A. Z. et al. Quantitative mapping of fluorescently tagged cellular proteins using FCS-calibrated four-dimensional imaging. *Nat. Protoc.* **13**, 1445–1464 (2018).
- Schindelin, J. et al. Fiji: an open-source platform for biological-image analysis. *Nat. Methods* **9**, 676–682 (2012).
- Kremer, J. R., Mastronarde, D. N. & McIntosh, J. R. Computer visualization of three-dimensional image data using IMOD. *J. Struct. Biol.* **116**, 71–76 (1996).
- Hagen, W. J. H., Wan, W. & Briggs, J. A. G. Implementation of a cryo-electron tomography tilt-scheme optimized for high resolution subtomogram averaging. *J. Struct. Biol.* **197**, 191–198 (2017).

Acknowledgements

We are grateful to the Advanced Light Microscopy Facility and the cryo-Electron Microscopy Platform at the European Molecular Biology Laboratory (EMBL), especially to S. Terjung, A. Halavatyi, S. Schnorrenberg, W. Hagen and F. Weis, and to G. Celetti for the kind gift of purified GFP protein. The Alvéole Lab company members M. Akuyz, G. Peyret, L. Siquier and L. Bonnemay are acknowledged for advice and helpful discussions. J.M. is grateful to the EMBL for funding. M.T.-N. was supported by a fellowship from the EMBL Interdisciplinary (EI3POD) program under Marie Skłodowska-Curie Actions COFUND (no. 664726). This project received funding from the European Research Council: ERC 3DCellPhase (grant no. 760067) to J.M., ERC ICEBERG (grant no. 771599) to M.T. and ERC AAA (grant no. 741773) to L.B.

Author contributions

M.T.-N., L.B., M.T. and J.M. conceived the study. M.T.-N., M.T. and J.M. designed the experiments. M.T.-N., I.Z., F.S. and J.M. performed experiments. M.T.-N. and J.M. made the figures and wrote the manuscript, with contributions from all authors. M.T. and J.M. supervised the work.

Competing interests

Authors are listed as inventors on a patent application relating to this report.

Additional information

Supplementary information is available for this paper at <https://doi.org/10.1038/s41592-019-0630-5>.

Correspondence and requests for materials should be addressed to J.M.

Peer review information Rita Strack was the primary editor on this article and managed its editorial process and peer review in collaboration with the rest of the editorial team.

Reprints and permissions information is available at www.nature.com/reprints.

Reporting Summary

Nature Research wishes to improve the reproducibility of the work that we publish. This form provides structure for consistency and transparency in reporting. For further information on Nature Research policies, see [Authors & Referees](#) and the [Editorial Policy Checklist](#).

Statistics

For all statistical analyses, confirm that the following items are present in the figure legend, table legend, main text, or Methods section.

n/a Confirmed

- The exact sample size (n) for each experimental group/condition, given as a discrete number and unit of measurement
- A statement on whether measurements were taken from distinct samples or whether the same sample was measured repeatedly
- The statistical test(s) used AND whether they are one- or two-sided
Only common tests should be described solely by name; describe more complex techniques in the Methods section.
- A description of all covariates tested
- A description of any assumptions or corrections, such as tests of normality and adjustment for multiple comparisons
- A full description of the statistical parameters including central tendency (e.g. means) or other basic estimates (e.g. regression coefficient) AND variation (e.g. standard deviation) or associated estimates of uncertainty (e.g. confidence intervals)
- For null hypothesis testing, the test statistic (e.g. F , t , r) with confidence intervals, effect sizes, degrees of freedom and P value noted
Give P values as exact values whenever suitable.
- For Bayesian analysis, information on the choice of priors and Markov chain Monte Carlo settings
- For hierarchical and complex designs, identification of the appropriate level for tests and full reporting of outcomes
- Estimates of effect sizes (e.g. Cohen's d , Pearson's r), indicating how they were calculated

Our web collection on [statistics for biologists](#) contains articles on many of the points above.

Software and code

Policy information about [availability of computer code](#)

Data collection

ZenBlack v2.3 SP1 v14.0.15.201 (Zeiss)
 Zen (blue edition) 2.3 v2.3.69.1000 (Zeiss)
 Leonardo software v4.12 (Alvéole Lab)
 Micro-manager v1.4.22 (open source)
 ImageJ v1.48 (open source)
 Olympus FV 10-ASW software v04.02.03.02 (Olympus)
 MyPic VBA macro (Politi et al. 2018. Nat Protoc 13, 1445-1464)
 Serial EM v3.7.2 (open source)
 MAPS v3.3 software
 CellSens Entry 1.9 (Olympus)

Data analysis

Inskape v0.92 (open source)
 Fiji (ImageJ) v2.0.0-rc-59/1.51k (open source)
 ZenBlack v2.3 SP1 14.0.15.201 (Zeiss)
 IMOD package v4.9.0 (open source)
 ZenBlack v2.3 SP1 v14.0.15.201 (Zeiss)
 Zen (blue edition) 2.3 v2.3.69.1000 (Zeiss)

For manuscripts utilizing custom algorithms or software that are central to the research but not yet described in published literature, software must be made available to editors/reviewers. We strongly encourage code deposition in a community repository (e.g. GitHub). See the Nature Research [guidelines for submitting code & software](#) for further information.

Data

Policy information about [availability of data](#)

All manuscripts must include a [data availability statement](#). This statement should provide the following information, where applicable:

- Accession codes, unique identifiers, or web links for publicly available datasets
- A list of figures that have associated raw data
- A description of any restrictions on data availability

The authors declare that the data supporting the findings of this study are available within the paper and its supplementary information files. The raw data study are available from the corresponding author upon reasonable request.

Field-specific reporting

Please select the one below that is the best fit for your research. If you are not sure, read the appropriate sections before making your selection.

- Life sciences Behavioural & social sciences Ecological, evolutionary & environmental sciences

For a reference copy of the document with all sections, see nature.com/documents/nr-reporting-summary-flat.pdf

Life sciences study design

All studies must disclose on these points even when the disclosure is negative.

Sample size	Statistical methods were not used to predetermine sample size. Sample sizes were chosen according to previous experience in similar experimental setups. Briefly, for conventional defocus data, a total of 30 tomograms were acquired on the peripheral areas of 13 micropatterned cells. A total of 31 VPP tomograms were acquired from 8 wedges, equivalent to 8 cells grown on crossbow-, cross-, dumbbell-, oval-, and disk-shape micropatterns. The technical procedure as well as the results from these experiments were reproducible: at least 60 micropatterned grids have been seeded with either HeLa or RPE1 cells obtaining reproducible results with cells settling and adhering to the micropatterned areas.
Data exclusions	None.
Replication	All reported experiments have been repeated at least three times with independent samples (unless indicated otherwise). All experimental results shown were reproducible. No exclusion criteria were pre-established.
Randomization	No experimental groups were formed/compared. Data was collected randomly in each set of experiments.
Blinding	The researchers were not blinded to sample identity, as targeting the specific biological specimen is highly relevant for using the developed method described in the manuscript, for example, when selecting cells grown on specific complex micropatterned shapes for further for cryo-ET and/or cryo-FIB milling.

Reporting for specific materials, systems and methods

We require information from authors about some types of materials, experimental systems and methods used in many studies. Here, indicate whether each material, system or method listed is relevant to your study. If you are not sure if a list item applies to your research, read the appropriate section before selecting a response.

Materials & experimental systems

n/a	Involved in the study
<input checked="" type="checkbox"/>	<input type="checkbox"/> Antibodies
<input type="checkbox"/>	<input checked="" type="checkbox"/> Eukaryotic cell lines
<input checked="" type="checkbox"/>	<input type="checkbox"/> Palaeontology
<input checked="" type="checkbox"/>	<input type="checkbox"/> Animals and other organisms
<input checked="" type="checkbox"/>	<input type="checkbox"/> Human research participants
<input checked="" type="checkbox"/>	<input type="checkbox"/> Clinical data

Methods

n/a	Involved in the study
<input checked="" type="checkbox"/>	<input type="checkbox"/> ChIP-seq
<input checked="" type="checkbox"/>	<input type="checkbox"/> Flow cytometry
<input checked="" type="checkbox"/>	<input type="checkbox"/> MRI-based neuroimaging

Eukaryotic cell lines

Policy information about [cell lines](#)

Cell line source(s)	Wild type HeLa Kyoto. Poser et al, 2008. Nat. Methods 5, 409–415. (obtained from Hyman lab, MPI-CBG, Germany) HeLa Kyoto B-tubulin-GFP, H2B-mCherry. Poser et al, 2008. Nat. Methods 5, 409–415 (obtained from Hyman lab, MPI-CBG, Germany)
---------------------	--

RPE1 LifeActGFP. Vignaud, T. et al. 2012. J Cell Sci 125, 2134-2140 (They and Blanchoin Lab, Laboratoire de Physiologie Cellulaire et Végétale, Université Grenoble-Alpes/CEA/ CNRS/INRA, Grenoble, France).

Authentication

Cells were not authenticated after obtained from the source.

Mycoplasma contamination

All cell lines were tested negative for mycoplasma contamination (using Eurofins service)

Commonly misidentified lines
(See [ICLAC](#) register)

No commonly misidentified cell lines were used.